CHEMISTRY OF MATERIALS

Article

pubs.acs.org/cm

Interfacial Oxygen Vacancies as a Potential Cause of Hysteresis in Perovskite Solar Cells

Fan Zhang,[†,¶] Wei Ma,[†,¶] Haizhong Guo,[*,†] Yicheng Zhao,[‡] Xinyan Shan,[†] Kuijuan Jin,[†,§] He Tian,[∥] Qing Zhao,[‡,§] Dapeng Yu,[‡,§] Xinghua Lu,[†,§] Gang Lu,[*,⊥] and Sheng Meng[*,†,§]

[†]Beijing National Laboratory for Condensed Matter Physics, and Institute of Physics, Chinese Academy of Sciences, Beijing, 100190, P. R. China

[‡]Peking University, Beijing, 100871, P. R. China

[§]Collaborative Innovation Center of Quantum Matter, Beijing, 100190, P. R. China

[∥]Department of Materials Science & Engineering, State Key Laboratory of Silicon Materials, Zhejiang University, Hangzhou, Zhejiang 310027, P. R. China

[⊥]Department of Physics and Astronomy, California State University Northridge, Northridge, California 91330-8268, United States

Supporting Information

ABSTRACT: Organometal halide perovskite solar cells (PSCs) have emerged as one of the most promising photovoltaic technologies with efficiencies exceeding 20.3%. However, device stability problems including hysteresis in current−voltage scans must be resolved before the commercialization of PSCs. Transient absorption measurements and first-principles calculations indicate that the migration of oxygen vacancies in the TiO_2 electrode under electric field during voltage scans contributes to the anomalous hysteresis in PSCs. The accumulation of oxygen vacancies at the electrode/perovskite interface slows down charge extraction while significantly speeding up charge recombination at the interface. Moreover, nonadiabatic molecular dynamics simulations reveal that the charge recombination rates at the interface depend sensitively (with 1 order of magnitude difference) on the locations of oxygen vacancies. By intentionally reducing oxygen vacancies in the TiO_2 electrode, we substantially suppress unfavorable hysteresis in the PSC devices. This work establishes a firm link between microscopic interfacial structure and macroscopic device performance of PSCs, providing important clues for future device design and optimization.

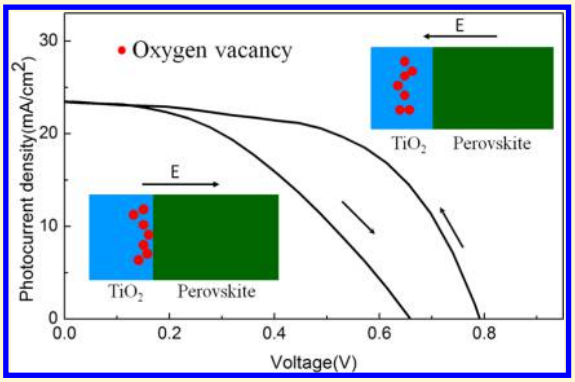

INTRODUCTION

Organic/inorganic trihalide lead based perovskite materials have attracted worldwide attention for their promising potential in photovoltaic and optoelectronic applications.[1−3] They have many desirable attributes such as low-cost, facile synthesis, high visible absorption, and long carrier diffusion lengths that are ideal for photovoltaic applications.[4−6] In the past few years, tremendous efforts were carried out for the optimization of the devices, including the development of novel light-harvesting[7,8] and carrier transport materials[9,10] as well as the improvement of perovskite film quality via new synthetic methods.[11−13] The state-of-the-art perovskite solar cell (PSC) incorporates either nanocrystalline or compact TiO_2 to facilitate electron transport and to enhance long-term stability,[14,15] accentuating the essential role of TiO_2 layers. Recently, the PSC with a novel light-harvesting layer has reached a record efficiency of 20.3%,[16] approaching that of thin film CdTe and $CuInGaSe_2$ solar cells.

Despite significant progress, critical problems remain to be resolved before PSCs could enter the marketplace. In particular, anomalous hysteresis and device stability are among the most challenging issues. It has been observed that the perovskite devices exhibit significant hysteresis during opposite voltage scanning directions, casting doubts on the reliability and stability of this technology. The hysteresis exists in both planar device structure and those with mesoporous scaffolds.[17] The hysteresis is strongly influenced by the scanning rate and the perovskite crystal size.[18,19] Using piezoforce microscopy, Padture et al. directly observed ferroelectric domains induced by $CH_3NH_3^+$ in high-quality $CH_3NH_3PbI_3$ thin films and demonstrated its contribution to the hysteresis.[20] Walsh et al. established a link between ferroelectric domains and hysteresis by using first-principles modeling.[21] However, it is under heavy debate whether ferroelectricity is related to hysteresis, mainly due to its incomparable time scale with the operation time of devices.[22−25] Now many works believe trap states or ion migration of perovskite are responsible for hysteresis. For

Received: October 15, 2015
Revised: January 13, 2016
Published: January 13, 2016

DOI: 10.1021/acs.chemmater.5b04019
Chem. Mater. 2016, 28, 802−812

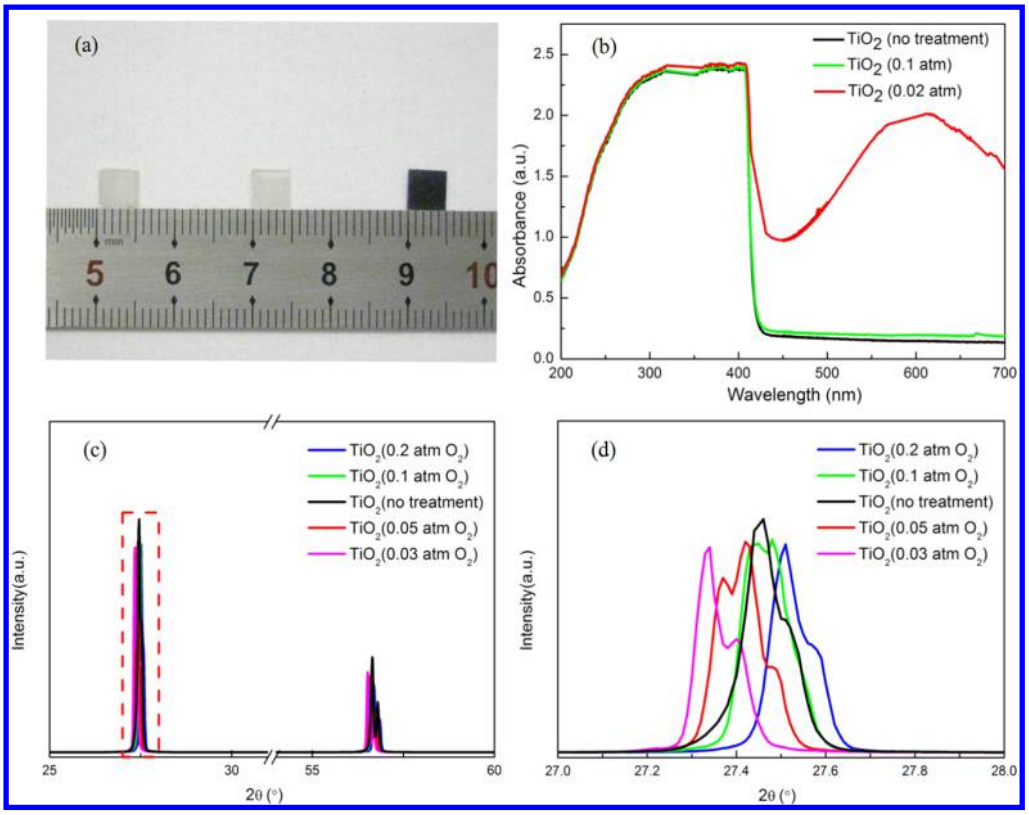

Figure 1. (a) TiO_2 single crystals with different V_O densities are transparent or blue. (From left to right: TiO_2 without treatment, annealed at 0.1 and 0.02 atm oxygen pressure.) (b) UV−vis absorption spectra of different TiO_2 single crystals. (c) XRD patterns of pure TiO_2 and TiO_2 treated with various amounts of oxygen vacancies. (d) An enlarged view of the spectra in (c).

example, by fullerene passivation in planar PSCs, Huang et al. and Sargent et al. were able to eliminate hysteresis. It was hence speculated that defects in perovskite lattice and surface could trap carriers, leading to hysteresis.[26−28] More serious hysteresis was observed after applying constant electric field to PSC devices. The switchable photovoltaic effect was explained by ion migration within the perovskite layer.[29,30]

Recently, Snaith et al. showed theoretically that both ion migration and electronic charge traps, serving as recombination centers, were responsible for adverse hysteresis in PSC.[31] The paper does not explain the details of mobile ions or carrier traps. By doping zirconium or lithium into the TiO_2 electrode, Ginger et al. and Im et al. improved the power conversion efficiency (PCE) and suppressed hysteresis of perovskite solar cells.[32,33] Therefore, carrier traps in TiO_2 is also an important factor influencing the anomalous hysteresis in PSC. To further investigate the microscopic origins of hysteresis and give guidance to solve the hysteresis problem, detailed understanding of the interfacial photophysics in PSC is urgently needed.

In this work, we systematically investigate how interfacial oxygen vacancies (V_O) may influence the electron transfer rates, thus resulting in anomalous hysteresis in PSCs. By employing a combination of transient absorption (TA) spectra, time-resolved photoluminescence (PL) spectra and first-principles nonadiabatic molecular dynamics (NAMD)[34,35] based on time-dependent density-functional theory (TDDFT), we find that oxygen vacancies at the TiO_2 surface could act as traps for photoexcited electrons. With a higher concentration of oxygen vacancies, photoexcited electron injection from perovskite to TiO_2 is slowed down, while the charge recombination rate is *dramatically* increased. NAMD simulations show that the electron−hole recombination dynamics at the interface depends strongly on the position of oxygen vacancies. These vacancies could migrate during the voltage scans, resulting in contrasting device performances depending on the scanning directions. Therefore, the interfacial oxygen vacancies are identified as one of the microscopic origins of anomalous hysteresis, which have been largely ignored up to now. More importantly, we show that the hysteresis can be suppressed by reducing the interfacial oxygen vacancies.

RESULTS

Controlling Oxygen Vacancy Density. Previous works have shown that defects in bulk and perovskite surface could trap carriers, giving rise to anomalous hysteresis in TiO_2 PSCs.[26−28] Here we find that oxygen vacancies (V_O) in electron transport layer TiO_2 have the same detrimental effect. First of all, a link between V_O and hysteresis should be confirmed. A straightforward way is to control the V_O density and see whether the hysteresis of PSCs is influenced. In this work, we intentionally manipulated V_O density in TiO_2 mainly by annealing it in different atmosphere or by plasma treatment.

The existence of oxygen vacancies in treated TiO_2 can be characterized by UV−vis absorption spectra and XRD. Here we adopt the TiO_2 single crystal as a simple model. For TiO_2 without any treatment, it has an optical bandgap of 3 eV. Therefore, it cannot absorb visible light (Figure 1a,b). When oxygen vacancies are introduced into TiO_2, electrons trapped in localized states within the bandgap can be excited to the conduction band, leading to strong absorption in the visible range (Figure 1a,b).

DOI: 10.1021/acs.chemmater.5b04019
Chem. Mater. 2016, 28, 802−812

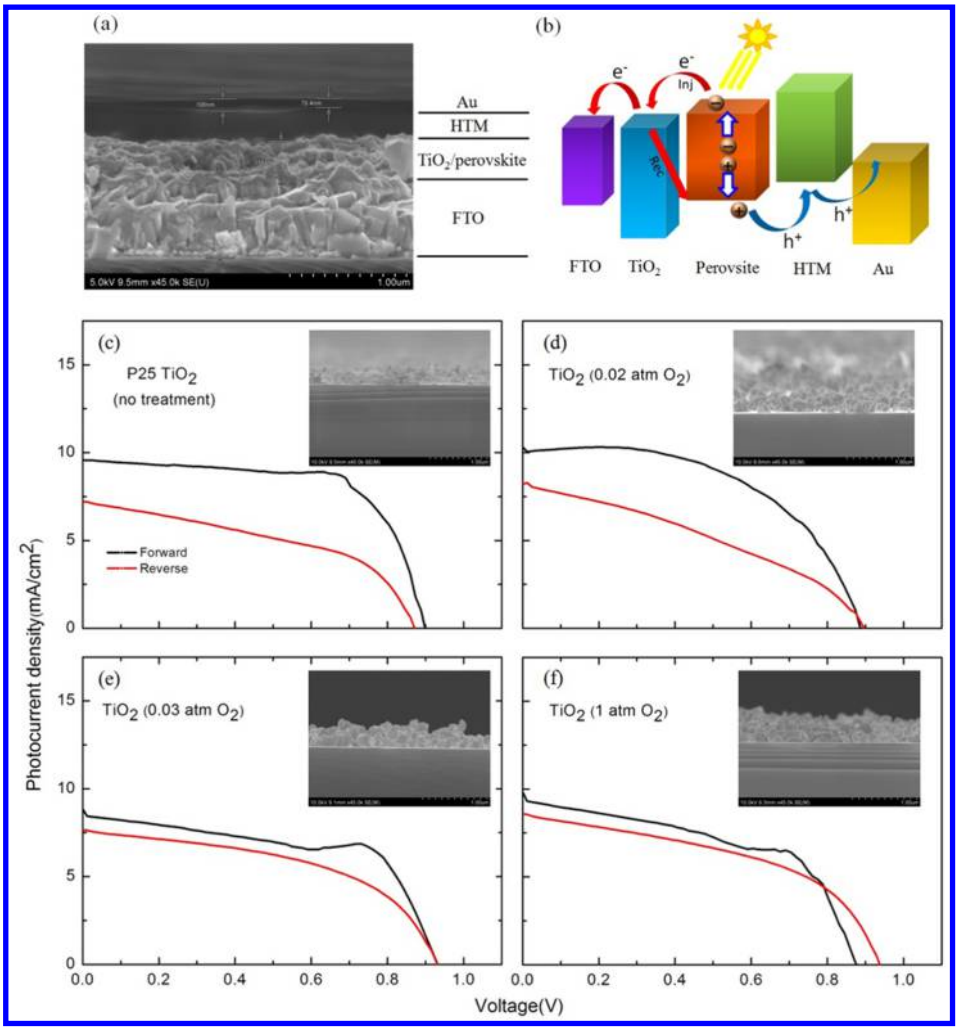

Figure 2. (a): Cross-sectional image of perovskite solar cell device based on mesoporous TiO_2. (b): Diagram of charge transfer process in devices. (c)−(f): The stabilized current−voltage (I−V) curves for perovsktie solar cells with TiO_2 photoanode annealed at different oxygen pressure, measured under AM 1.5G (100 mW/cm^2) illumination. (c) P25 TiO_2, TiO_2 pretreated in oxygen pressure of 0.02 atm (d), 0.03 atm (e), and 1 atm (f). Insets are SEM images of TiO_2 nanocrystals.

However, when Vo density is low, UV−vis absorption measurement cannot distinguish the difference between TiO_2 treated in high oxygen pressures from P_{O_2} = 0.03 to 0.2 atm by heating at 900 °C for 24 h (P_{O_2} is defined as oxygen partial pressure, 1 atm =1.01 × 10^5 Pa). Figure 1b shows an example for TiO_2 annealed in P_{O_2} = 0.1 atm (green curve). Its absorption spectrum nearly overlaps with TiO_2 perfect crystal without any treatment.

We apply XRD to distinguish the small differences between TiO_2 substrates upon heat treatments under different P_{O_2}. The XRD patterns for TiO_2 treated under different P_{O_2} are shown in Figure 1 (Figure 1c for wide angle XRD and Figure 1d is an enlarged view of Figure 1c between 27.0° and 28.0°). From Figure 1c we find that all the samples exhibit pure rutile phase, suggesting that oxygen doping does not change the phase of TiO_2. The peak at about 27.4° is assigned to the rutile (110) diffraction. There is an obvious shift in the peak position, which indicates that there is a change in the spatial separation distance between neighboring TiO_2 (110) lattice planes. Using the Bragg equation, the (110) crystal plane spacing is calculated to be enlarged from 3.242 to 3.262 Å with oxygen pressure decreasing from 0.2 to 0.03 atm. It has been reported that oxygen removal lead to repelling between nearest Ti cations and the increase in lattice spacing.[36,37] Our result is in good accordance with this trend.

Figure 1d shows that a large amount of oxygen vacancies naturally exist in commercial TiO_2 single crystals without any treatment (black curve). Natural TiO_2 single crystal roughly corresponds to the samples treated at an oxygen pressure of ∼0.1 atm. After annealing in P_{O_2} = 0.2 atm atmosphere, V_O sites can be partly filled. The V_O reduction or addition can be also characterized by electrical conductivity measurement. Resistivity of commercial TiO_2 is determined to be 9.3 × 10^3 Ω·m by four-probe measurement. The value for TiO_2 (P_{O_2} = 0.02 atm) is 8.6 × 10^{-3} Ω·m, indicating effectively n-type doping. For TiO_2 annealed at 0.2 atm oxygen pressure, its resistivity is beyond the measurement range, much higher than the above two cases. The result matches well with previous work,[38] suggesting that the Vo density can be controlled intentionally.

Influence of Oxygen Vacancies on Device Hysteresis. Inspired by the fact that oxygen vacancies in TiO_2 can be controlled, we move to the second step to see whether the hysteresis of PSCs can be influenced by V_O density. Figure 2a

DOI: 10.1021/acs.chemmater.5b04019
Chem. Mater. 2016, 28, 802−812

Table 1. Performance Characteristics of Perovskite Solar Cells Based on Nanocrystalline TiO_2 with Different V_O Densities

cell	oxygen pressure (atm)	sweep direction	V_{oc} (V)	J_{sc} (mA/cm^2)	FF	η (%)	hysteresis index
#1	no treatment	FS[a]	0.90	9.6	0.67	5.8	2
		RS[b]	0.87	7.2	0.46	2.9	
#2	0.02	FS	0.89	10.0	0.54	4.8	1.85
		RS	0.89	8.1	0.35	2.6	
#3	0.03	FS	0.93	8.5	0.64	5.0	1.43
		RS	0.93	7.6	0.50	3.5	
#4	1	FS	0.88	9.3	0.54	4.5	1.18
		RS	0.93	8.5	0.48	3.8	

[a]FS: forward scan, from V_{oc} to J_{sc}; [b]RS: reverse scan, from J_{sc} to V_{oc}.

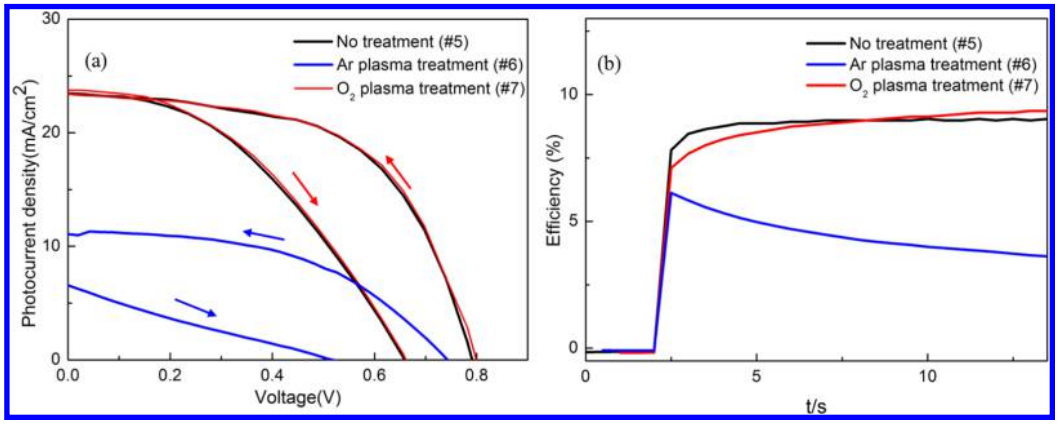

Figure 3. (a) Stabilized current−voltage (I−V) curves for perovsktie solar cells with TiO_2 compact layer treated by plasma, measured under AM 1.5G (100 mW/cm^2) illumination. Arrows represent scanning direction. (b) Power conversion efficiency as a function of time for the same cell in (a) held close to maximum power point forward bias.

Table 2. Performance Characteristics of Planar Perovskite Solar Cells Based on Compact TiO_2 with Different Plasma Treatments

cell	treatment	sweep direction	V_{oc} (V)	J_{sc} (mA/cm^2)	FF	η (%)	hysteresis index
#5	no treatment	FS[a]	0.79	23.4	0.57	10.58	1.66
		RS[b]	0.66	23.4	0.41	6.39	
#6	Ar	FS	0.74	11.3	0.49	4.07	5.34
	plasma	RS	0.51	6.6	0.23	0.76	
#7	O_2	FS	0.80	23.4	0.57	10.63	1.63
	plasma	RS	0.65	23.7	0.42	6.53	

[a]FS: forward scan, from V_{oc} to J_{sc}; [b]RS: reverse scan, from J_{sc} to V_{oc}.

shows a typical structure of the mesoporous perovskite solar cell (PSC) devices. The TiO_2 nanocrystalline film is doped with oxygen vacancies by sintering the film at 500 °C in different oxygen atmosphere. Although the lower annealing temperature is adopted here, XRD confirms the crystal lattice changes for the treated nanocrystalline TiO_2 (Figure S1). The higher the oxygen pressure, the lower the V_O density would be resulted. Key parameters of the devices including short-circuit photocurrent J_{sc}, open-circuit voltage V_{oc}, and fill factors (FF) are listed in Table 1, together with the overall sunlight-to-electricity conversion efficiency (η) of the solar cell devices. All I−V curves were recorded until the devices reached a stable state under illumination (Figure 2). The scanning rate is moderate being 0.15 V/s. Forward scan is defined as scanning from V_{oc} to J_{sc}, while the reverse scan is scanning from J_{sc} to V_{oc}.

When P25 nanocrystalline TiO_2 is introduced as electron extraction layer and scaffold, the PSC device reaches an efficiency of η = 9% (forward scan), then its efficiency is stabilized at ∼6% under one sun illumination. Other devices differ from cell #1 by substituting the P25 TiO_2 with annealed TiO_2 samples. As a result, efficiency of cells with modified TiO_2 decreased to be ∼5% (highest value, see Table 1). The reduction can be explained by the appearance of larger size of nanoparticles and undesirable three-dimensional assembly of nanoparticles. Insets in Figure 2c−f show that TiO_2 nanoparticles grow to be over 100 nm after annealing, much larger than P25. These planar-like devices have lower efficiency than cell #1 under our experimental conditions.

The hysteresis index is defined as $\eta_{forward}/\eta_{reverse}$. In Table 1, hysteresis index values are listed together with photovoltaic parameters depending on scan direction. For devices with larger amounts of V_O (P_{O_2} = 0.02 atm), they show larger hysteresis index of 1.85 compared with those ($\eta_{reverse}/\eta_{forward}$ = 1.18) with less V_O (P_{O_2} = 1 atm). It is noted that I−V hysteresis becomes less pronounced as the V_O density decreased. Since parameters of all devices were controlled to be the same except cell #1 with smaller TiO_2 crystalline size, it is reasonable to attribute the reduced hysteresis to less V_O sites within TiO_2. Interestingly, cell #1 with P25 TiO_2 also shows severe hysteresis. Compared

DOI: 10.1021/acs.chemmater.5b04019
Chem. Mater. 2016, 28, 802−812

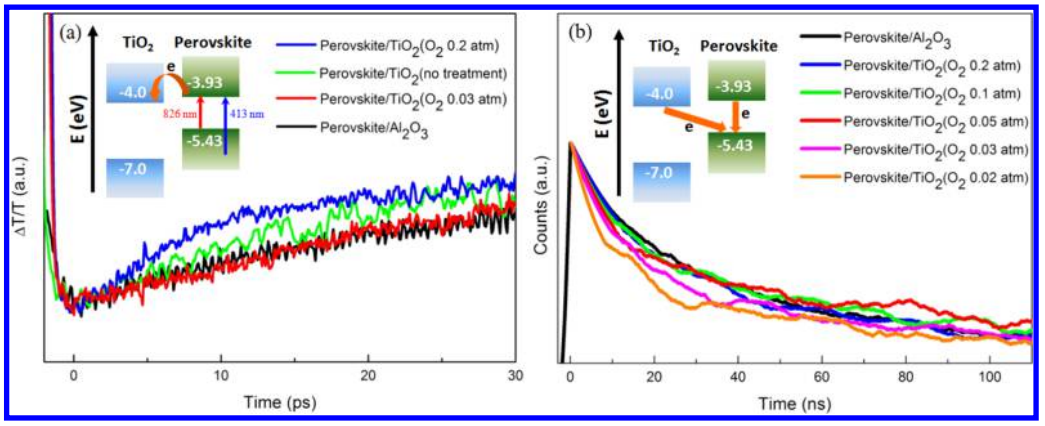

Figure 4. (a) Kinetic curves of transient absorption. Perovskite is deposited on Al_2O_3 (black), TiO_2 without treatment (green), TiO_2 calcined at 0.2 atm (blue), and 0.03 atm O_2 (red), respectively. Inset shows schematic diagram of electron injection process. (b) Time-resolved PL measurements taken at emission wavelength of perovskite on different substrates. Inset shows schematic diagram for electron relaxation and recombination processes.

with cell #4, it is clear that we almost eliminate hysteresis by reducing V_O amounts in TiO_2.

To avoid the complex structure of mesoporous TiO_2 layer, we also investigate the effect of V_O on hysteresis in planar PSCs. In this type of device, the mesoporous TiO_2 layer is removed. Oxygen vacancies in the compact TiO_2 layer were produced (reduced) by Ar (O_2) plasma, which is well-known as a surface treatment technique.[39,40] The performance of planar PSC devices is shown in Figure 3 and Table 2, together with their hysteresis index listed.

When compact TiO_2 without any treatment is applied in the PSC device, the device reaches an efficiency of η = 10.58% (forward scan, cell #5), and its efficiency is stabilized at ~8.9% under one sun illumination (Figure 3b). For cell #6, V_O density in TiO_2 is increased by Ar plasma treatment,[41,42] confirmed by XRD (Figure S2). It is obvious that efficiency of cells with a high density of V_O dramatically decreases to 4.07%, with much larger hysteresis index (5.34) compared to cell #5 (1.66). More importantly, its maximum power output undergoes a fast decay in less than 10 s, suggesting a detrimental effect of oxygen vacancies. For cell #7, its V_O density is reduced by O_2 plasma,[39,43] leading to a slightly higher efficiency (forward scan, 10.63%) and lower hysteresis index (1.63). The real efficiency of cell #7 is determined to be 9.3% by stabilized power measurement (Figure 3b). Comparing cell #7 with #5, it is clear that the removal of oxygen vacancy at TiO_2 surface improve the device performance.

All planar PSCs show larger hysteresis than their mesoporous counterparts, which can be easily understood by insufficient charge extraction of TiO_2.[44] Still, performance of planar perovskite solar cell strongly proves that V_O in TiO_2 is a potential cause of hysteresis, which is the same as mesoporous cells.

Ultrafast Charge Dynamics between Perovskite and TiO_2. The role of these V_O sites in TiO_2 can be investigated by transient absorption (TA) and time-resolved PL measurement. Perovskite $CH_3NH_3PbI_3$ film was deposited on single-crystal TiO_2 substrate pretreated with different V_O densities. In TA measurement, pulse with a wavelength of 826 nm (1.5 eV) was used to excite electrons in perovskite and its response to 413 nm light was shown in Figure 4a. Fitting the kinetics for the transient absorption signal of light at 413 nm shows a time constant of 10–20 ps. The decay behavior originates from photoexcited electrons in perovskite conduction band, judging from the measured ultrafast time scale.[45] Because the photon energy of 413 nm is at the band edge excitation of TiO_2, we exclude the absorption features of TiO_2 by subtracting the optical response of pure TiO_2 sample. TA signal of $CH_3NH_3PbI_3/Al_2O_3$ is shown as a reference (black curve) in Figure 4a. As a wide-gap insulator (bandgap 7–9 eV), Al_2O_3 does not respond to 826 and 413 nm excitations.[46] Therefore, the signal decay for perovskite/Al_2O_3 is attributed to charge transfer process within perovskite crystal, mostly like to defect-induced trap states and grain boundaries.[47]

When Al_2O_3 is replaced by semiconducting TiO_2 without treatment, the decaying behavior in transient absorption introduced by excited electrons is shown in Figure 4a (red curve). The 11 ps process is faster than electron transfer rate in perovskite itself, which can be explained by additional channel for electrons flowing from perovskite to TiO_2 conduction band edge, namely, the photoelectron injection. As a result, TiO_2 acts as an electron transfer acceptor for photogenerated electrons in perovskite.

Figure 4a and Table 3 show the influence of V_O density on charge injection rate. For each case, we measure transient signal at more than 10 points and average the time constants in Table 3. Low oxygen pressure during annealing leads to more oxygen vacancies. It is clear that slower injection rates result from more oxygen vacancies. For TiO_2 with a large amount of V_O sites (P_{O_2} = 0.03 atm), the time constant is even comparable with that of perovskite/Al_2O_3 (Figure 4a).

Table 3. Kinetic Parameters for Electron Injection from Perovskite to Different TiO_2 Substrates Measured by TA Setup

substrate	TiO_2 (O_2 0.2 atm)	TiO_2 (O_2 0.1 atm)	TiO_2 (O_2 0.03 atm)	Al_2O_3
τ (ps)	11	13	20	~ 20

Time-resolved PL has been performed to investigate the carrier recombination rate at $CH_3NH_3PbI_3/TiO_2$ interface. Figure 4b shows the PL decay curve of perovskite on different substrates. The instrumental response curve has already been cut off. Fitting the decaying signal with double exponential function gives 13 and 71 ns time constant for $CH_3NH_3PbI_3/Al_2O_3$ heterointerface (black curve). The faster component is attributed to recombination at grain boundaries as shown in

DOI: 10.1021/acs.chemmater.5b04019
Chem. Mater. 2016, 28, 802–812

Table 4. PL Lifetime of Perovskite on Different Substrates

substrate	Al_2O_3	TiO_2 (O_2 0.2 atm)	TiO_2 (O_2 0.1 atm)	TiO_2 (O_2 0.05 atm)	TiO_2 (O_2 0.03 atm)	TiO_2 (O_2 0.02 atm)
τ (ns)	71	32.7	32	28.6	27.2	24.6

Figure S3.[47] The 71 ns process is designated to be the intrinsic lifetime of photo excited carriers, which is shorter than previously reported values[4,48,49] due to the differences in experimental setup.

When TiO_2 is used as the substrate, photoexcited electrons in $CH_3NH_3PbI_3$ will be injected into TiO_2. TA measurement demonstrates that the injection process happens within a time scale of picoseconds, which is much faster than the instrument response of PL measurements (nanosecond scale). Afterward, injected electrons would have a probability to recombine with the holes in perovskite, which produces the exponential decaying signals in the PL intensity.

We find that the recombination rate is significantly influenced by V_O densities. Table 4 summarizes time constants for electron−hole recombination process for perovskite deposited on TiO_2 with different V_O densities. All perovskite films were fabricated with the same parameters. The film thicknesses on all substrates are 200 ± 10 nm, which are essentially the same within the measurement error. It is clear that more oxygen vacancies lead to faster recombination rates at the interface.

Above data suggest that oxygen vacancies in TiO_2 are harmful for carrier transport at TiO_2/perovskite interface, both for injection and recombination. However, it was reported recently that TiO_2 may passivate the original surface states in perovskite, thus enhancing PL lifetime compared to perovskite itself.[50] We have not observed this phenomenon for perovskite on single-crystal TiO_2.

Effects of Oxygen Vacancies on Electron Transfer using NAMD Simulations. To give a deeper insight into how oxygen vacancies of TiO_2 influence macroscopic hysteresis in current−voltage (I−V) scans, we investigate the effects of V_O on interfacial electron injection and electron−hole recombination using the fewest-switching-surface-hopping (FSSH) NAMD simulations.[34,35]

The FSSH method is based on the hypothesis that the time evolution of a wave packet through a potential-energy branching region can be approximated by an ensemble of independent semiclassical trajectories stochastically distributed among the branched surfaces. Electronic redistribution is achieved by allowing electronic hops between the potential energy surfaces according to a certain probability distribution determined by the nonadiabatic couplings.

In line with the experiments, we have placed a sheet of perovskite (containing 84 atoms) on top of the rutile TiO_2 (110) surface (with 96 atoms in six-atomic layers) to model the perovskite/TiO_2 heterointerface (Figure 5a). Five different sites of V_O (a, b, c, d, and e) at the interface between the perovskite/TiO_2 are considered (Figure 5a). The oxygen atoms in V_O-a and V_O-c are 2-fold bridging, whereas oxygen atoms in V_O-b, V_O-d and V_O-e are 3-fold coordinated. We note that the TiO_2 slab adopted here is thin, containing only surface and subsurface oxygen vacancies which are sufficiently close to the perovskite/TiO_2 interface or to TiO_2 surface. Although the thicker TiO_2 slab could be used in principle to obtain concrete data, it brings huge computational cost unaffordable in the present work.

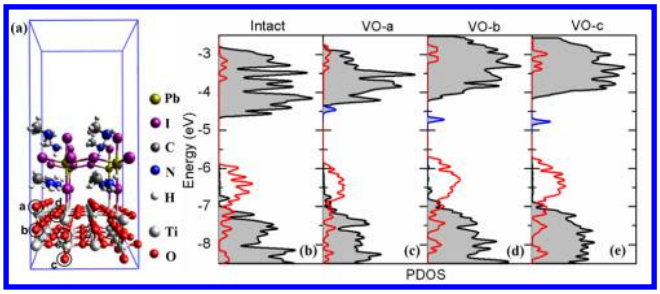

Figure 5. (a) Atomic structure of perovskite/TiO_2 rutile (110) interface. a, b, c, d, and e show five different atomic sites of oxygen vacancy in the TiO_2 substrate. a, b, and c are stable. d transfers to a during the structural optimization, whereas e transfers to c during the MD. (b−e) Projected density of states (PDOS) of TiO_2/peroskite with V_O located at different sites in TiO_2. The gray shadowed region shows the density of states for TiO_2 substrate, the red lines denote the density of states for perovskite layer, while the blue lines are the defect states of oxygen vacancies in TiO_2.

To justify the choice of our relatively thin TiO_2 slab model, we compare carefully our results with those reported in literature obtained with considerably thicker TiO_2. The calculated formation energy for the surface (site c here) and subsurface (site b) oxygen vacancy is 3.39 and 3.44 eV, respectively. These numbers are fairly close to those reported by Selloni et al., 3.68 and 3.99 eV, for the surface and subsurface V_O formation, respectively, using an 18-atomic-layer TiO_2(110) slab.[51] Moreover, the trend in V_O formation energies for the three sites are in the order of a > b > c; the energy difference between site a and site b is 190 meV, and that between site b and site c is 50 meV. This trend reproduces well that found by Selloni et al., where surface V_O (site c) has the lowest formation energy. Therein the energy difference between surface and subsurface oxygen vacancies is 310 meV, which is even larger than our results for site a and site b (190 meV), implying that the kinetic barrier for V_O to diffuse from the TiO_2/perovskite interface to the bulk may be even lower than that for V_O diffusion from TiO_2 surface to the bulk (0.6−0.7 eV)[51] thanks to the interface bonding between TiO_2 and the perovskite. Nevertheless, V_O diffusion could occur in both thin and thick TiO_2 slab models.

In addition, because we focused on electron dynamics of perovskite/TiO_2 heterointerface here, only the oxygen vacancies near interface are crucial for electron injection and electron−hole recombination at interface. Therefore, we believe the model of perovskite/TiO_2 layer adopted here is plausible to capture the essential physics for interface interactions and yield reasonable results.

We found oxygen vacancies at a, b, and c sites are stable (during both structural optimization and molecular dynamics simulations). In contrast, strongly affected by the interactions between perovskite and TiO_2 layer, oxygen vacancy at d and e sites are not stable: V_O-d is not a minimum on the potential energy surface, changing to V_O-a during structural optimization; although Vo-e is stable after structural relaxation, it turns into V_O-c during heating from 0 to 300 K in MD simulations. The site c is the most stable one with the vacancy formation energy

DOI: 10.1021/acs.chemmater.5b04019
Chem. Mater. 2016, 28, 802−812

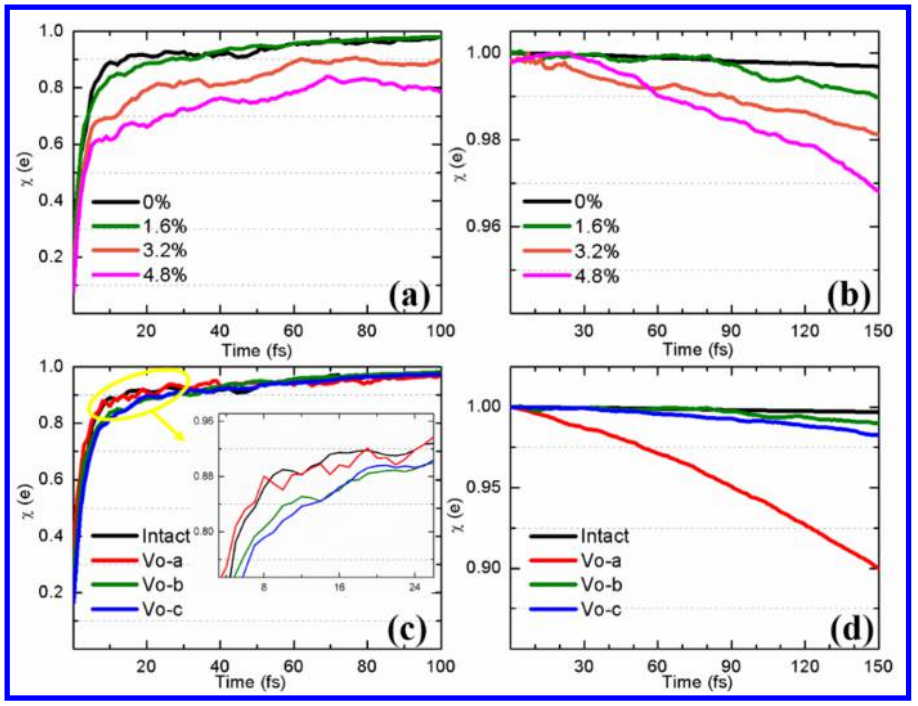

Figure 6. (a) Electron transfer fraction (χ) from the perovskite to the TiO_2 conduction bands as a function of time for different densities of V_O in TiO_2. (b) Electron transfer as a function of time during the recombination process for different densities of V_O in TiO_2. (c) Electron transfer fraction from the perovskite to the TiO_2 conduction bands as a function of time for intact TiO_2 and TiO_2 with V_O at different sites. (d) Electron transfer as a function of time during the recombination process for intact TiO_2 and TiO_2 with different V_O sites.

of 50 meV lower than that at the site b. The site a is the least stable one with the formation energy 190 meV higher than b.

It is well-known that point defects in a semiconductor can introduce defect states in the band gap. For TiO_2 with oxygen vacancies, an occupied defect level slightly below the TiO_2 conduction band edge is formed (Figure 5b-5e, ΔE = 0.17 eV for V_O-a, 0.58 eV for V_O-b, and 0.69 eV for V_O-c), corresponding to a donor state. The shallow donor state introduced by the V_O has been observed previously.[52−54] Although this donor state is occupied at the ground state, the electrons in this state can be thermally excited, and conversely, the excited electrons can relax back to the donor state.

Then we investigate the influence of different V_O densities on interfacial electron injection and electron−hole recombination. Several vacancy concentrations, including 0%, 1.6% (1 V_O in the simulation cell), 3.2%, and 4.8% are studied. Figure 6a shows the fraction of electrons injected from the perovskite to TiO_2 conduction bands in the presence of different oxygen vacancies concentration. By an exponential fit, the injection time scale is estimated as 3.83 fs for V_O density of 0%, 5.71 fs for 1.6%, 7.99 fs for 3.2%, and 11.14 fs for 4.8%. With the increase of the vacancy concentration, the electron injection rate decreases. The recombination dynamics for the different vacancy densities is shown in Figure 6b. As more oxygen vacancies introduce more electronic trap states, there is a dramatic increase in the charge recombination (or the electron back-transfer from TiO_2 conduction bands to the perovskite) rate. By a linear extrapolation, one can estimate the time scale for which all electrons are transferred back to the perovskite, defined as the time scale for the charge recombination. The time scale for recombination is estimated to be 46.59 ps for 0%, 13.65 ps for 1.6%, 5.16 ps for 3.2%, and 3.74 ps for 4.8%. Our computation results agree well with experimental data, that increasing the V_O densities in TiO_2 layer would introduce charge traps for interface electron transfer, thus significantly blocking electron injection from perovskite to TiO_2 substrate and dramatically facilitating charge recombination at the heterointerface. The difference in absolute values between theory and experiment is a result of ultrathin film thickness (~1 nm) and idealistic interface geometry assumed in theoretical modeling, while in experiments the electrons have to travel through much thicker perovskite film (~200 nm).

However, the above discussions can only demonstrate that V_O concentrations do affect the overall efficiency of PSC; why and how the densities of defects impact the adverse hysteresis are still unknown and need to be further explored. So we make further investigation on the influence of different V_O sites on interface charge transfer at perovskite/TiO_2 heterojunction. As shown in Figure 6c, compared with the perfect perovskite/TiO_2 interface (black line in Figure 6c), introducing of oxygen vacancies slightly slow down the electron injection dynamics across the interface (3.83 fs for the perfect TiO_2, 3.97 fs for the vacancy at site a, 5.71 fs at site b, and 5.35 fs at site c). When the position of V_O moves far away from interface, photoexcited electron transfer from perovskite to TiO_2 gradually slows down. The recombination dynamics for the different vacancy sites is shown in Figure 6d. V_O induced trap states dramatically accelerate back electron transfer from TiO_2 conduction bands to the perovskite. The recombination lifetime is strongly related to different V_O sites (46 ps for the intact TiO_2, 1 ps for site a, 14 ps for site b, and 10 ps for site, respectively. Note that the oxygen vacancy in site c is more like a surface vacancy (at TiO_2/vacuum interface), and therefore, the injection and recombination dynamics for site c might be different from the interface electronic dynamics of defects in deeper layer. However, the results for interface site a and subsurface site b is still meaningful. Therefore, faster electron−hole recombination

DOI: 10.1021/acs.chemmater.5b04019
Chem. Mater. 2016, 28, 802−812

takes place when V_O sites are located near the interface of heterojunction.

As the oxygen vacancies may migrate under the external electric field during the voltage scans,[55,56] different interfacial charge transfer and recombination rates may occur depending on the location of the vacancies. We thus infer that the oxygen vacancies could be one important origin of the anomalous hysteresis frequently observed in PSCs.

DISCUSSION

To verify this conjecture, we look back at PSC performance in Figure 2 and Figure 3. It is interesting to note that $\eta_{reverse}$ is lower than $\eta_{forward}$ in all cases, which is reasonable according to the above discussions. When the scan starts from V_{oc}, an external electric field pointing from perovskite layer to TiO_2 film is applied on the photovoltaic device, oxygen vacancies are thus transferred from perovskite/TiO_2 interface to deeper layers of TiO_2,[55,56] leading to a relatively slower recombination rate, therefore resulting in a higher power output. We note that the kinetic barrier for Vo migration in TiO_2 is 0.6−0.7 eV,[51] which can be overcome at room temperature. The directed diffusion of V_O toward or away from the interface region can be expected with the assistance of external electric field. When the scan starts from J_{sc}, an inverse electric field is applied, driving the oxygen vacancies transfer to the heterointerface, bringing about a faster interface recombination dynamics and generating worse power output. Based on this explanation, it is natural to deduce that less oxygen vacancies could lead to a more balanced device performance when the scanning direction is concerned.

The carrier trapping and detrapping mechanism also give us invaluable insight into the relationship between the V_O density and the hysteresis in PSC. Dynamic measurement and simulation have demonstrated that the presence of interfacial oxygen vacancies lead to carrier trapping for electrons flowing from perovskite to TiO_2. The explanation is valid for both single crystal and nanocrystalline TiO_2 (Figure S4). These traps are filled under forward bias working conditions, while they are emptied out under short-circuit conditions due to facile charge transfer to TiO_2, leading to poor operation until the traps are filled again.[26,44] The slow emptying and filling of traps (~0.01 s at room temperature[57]) is consistent with the long time scale of $I-V$ curve measuring.

Above discussion suggests that the reduction of oxygen vacancies in TiO_2 can effectively suppress unfavorable $I-V$ hysteresis of perovskite devices. In this work, the V_O sites act as traps for electrons injected from perovskite, facilitate charge recombination, and result in severe hysteresis. On the other hand, the presence of V_O sites improves the conductivity of TiO_2 as confirmed in electrical transport measurement. Therefore, a good balance must be retained between improved interfacial charge transfer efficiency and damaged transportation in bulk. According to simulation result, V_O at TiO_2/perovskite interface contributes more to hysteresis. Therefore, these V_O sites should be eliminated while bulk oxygen vacancy should be preserved to maintain the conductivity, as shown by O_2 plasma treated planar devices (Figure 3).

And it should be noted that dye-sensitized solar cell (DSC), which also applies TiO_2 as electron transport layer, does not exhibit hysteresis. The controversy can be explained by different coverage of the light absorber layer. In the PSC device, the perovskite nanocrystal contacts well with TiO_2 surface atom by atom (Figure 5a), while less than 10% surface atoms are linked to dye molecules in DSC. Based on this fact, we believe oxygen vacancy has a much larger effect in PSC than in DSC devices. A unique merit in the present work is that the stable performances in PSC devices are directly linked to the microscopic interface atomistic structures and electronic features at the perovskite/TiO_2 interface.

CONCLUSIONS

We present a combined spectroscopic and computational study on hysteresis phenomenon in perovksite solar cells. The oxygen vacancies in TiO_2 trap photoexcited electrons and migrate under electric field, resulting in different injection and recombination dynamics at interface, thus leading to unfavorable hysteresis. Annealing the nanocrystalline TiO_2 at 1 atm oxygen partial pressure or pretreating TiO_2 by O_2 plasma effectively fill the original V_O sites and suppress the $I-V$ hysteresis. We expect that our method is valid even after further optimization of PSC devices. The approaches such as applying constant electric field or annealing TiO_2 at controlled temperature will be employed to manipulate the location of oxygen vacancies, which may enhance and stabilize the device photovoltaic performance in a more precise way. The present study on the relationship between interfacial defects and photovoltaic performance provides new insights toward a complete understanding of perovskite solar cell working mechanisms at the microscopic scale.

METHODS

Perovskite Film Deposition. Perovskite film (doped with chlorine) was prepared by the following processes. First, rutile TiO_2 single crystals (Hefei Ke Jing Materials Technology Co., Ltd) were cleaned by acetone, deionized water, and ethanol. Then they were subjected to an O_3/ultraviolet treatment for 10 min. Following the cleaning procedure, TiO_2 crystals were coated with $PbI_2/PbCl_2$ by spin coating 0.5 M PbI_2 (99.999%, Aldrich) and 0.1 M $PbCl_2$ (99.999%, Aldrich) in *N*′,*N*-dimethylformamide (99.7%) at 4500 r.p.m. for 60 s and dried at 100 °C for 15 min. For transient absorption measurement, the concentration of $PbI_2/PbCl_2$ was reduced to be one-fifth. After that, perovskite was made by spin coating a solution of CH_3NH_3I (Dyenamo) in 2-propanol (10 mg/mL) at 1200 r.p.m. for 6s and 4500 r.p.m. for 60 s on PbI_2 film and dried at 100 °C for 10 min.

Perovskite Solar Cell Fabrication. FTO glasses were cleaned by sequential sonication in distilled water, acetone, and ethanol, and then treated in UV-Ozone cleaner for 15 min. To make the compact TiO_2 blocking layer, cleaned FTO glasses were coated with 0.15 M titanium tetraisopropanolate in ethanol by spin-coating method at 3000 r.p.m. for 60 s. The film was heated at 500 °C for 2 h. After the coated film was cooled to room temperature, the same process was repeated once. On the prepared dense TiO_2 layer, the nanocrystalline TiO_2 paste was deposited by a spin coating method, and the deposited film was annealed at 500 °C for 0.5 h. Thicknesses of the TiO_2 films were controlled to be 200 nm. Perovskite film was fabricated by a two-step deposition method. The parameters are the same as above. The hole transport material (HTM) consists of 67.7 mg of spiro-MeOTAD, (Luminescence Technology), 8.5 mg of bis(trifluoromethane) sulfonimide lithium salt (LiTFSI, 99.95%, Aldrich) and 0.027 mL of 4-*tert*-butylpyridine (TBP, 96%, Aldrich) in 1 mL of mixed solvent of

DOI: 10.1021/acs.chemmater.5b04019
Chem. Mater. 2016, 28, 802−812

chlorobenzene (99.7%) and acetonitrile (99.7%) (chlorobenzene:acetonitrile 20:1 v/v). The perovskite/TiO_2 films were coated with HTM solution using spin-coating method at 4000 r.p.m. for 30 s. For the counter electrode, 80 nm-thick Au film was deposited on the top of the HTM by thermal evaporation under 6×10^{-4} Pa vacuum. The device active area is 0.1 cm^2.

To fabricate planar perovskite solar cells, compact TiO_2 on FTO glasses are treated by Ar plasma for 3 min or O_2 plasma for 2 min (90 W). Then high-quality perovksite films were fabricated in a glovebox with well controlled humidity. Substrates were coated by spin coating 0.8 M $PbCl_2$ and 2.5 M CH_3NH_3I in *N*′,*N*-dimethylformamide at 2500 r.p.m. for 30 s and dried sequentially at 60 °C for 60 min, 100 °C for 50 min and 105 °C for 30 min.

Oxygen Vacancy Characterization. Oxygen vacancies were added or reduced by heating the single crystal at 900 °C for 24 h at an oxygen pressure of 0.02−1.0 atm. For the nanoparticle TiO_2 applied in devices, the annealing temperature was kept at 500 °C to avoid phase transformation. They were characterized by UV−vis absorption spectra and X-ray diffraction (XRD). Absorption spectra were measured by SpectraPro-500i UV−vis spectrometer. XRD patterns were collected on a Rigaku Smartlab 9000 X-ray diffractometer (Cu Kα) in the range of 10°−80°.

Ultrafast Dynamics Measurement. Dynamic measurements were carried out to characterize the electron injection and recombination process by using the femtosecond transient absorption setup (fs-TA) and time-resolved photoluminescence (PL) setup, respectively. For measuring charge injection dynamic with the fs-TA, a titanium/sapphire laser (Coherent, Ultra II) with a repetition rate of 80 MHz, and a pulse width of 150 fs was employed. The beam was separated into two parts. One part was used as the pump pulse to excite the sample. The other part was used to pass through a BaB_2O_4 crystal to generate light pulses with double frequency. In this study, 826 nm light (1.5 eV) was used for pumping and 413 nm (3.0 eV) for probing. Transmission spectrum difference ΔT at 413 nm between excited and ground state sample was recorded. Although 1.5 eV light may not be enough to excite electrons in perovskite directly from valence band to conduction band,[58] the tail states, thermal broadening, ultrashort pulses, and two-photon effects can make the transition possible.[59,60] For convenience, we still focus on electrons at conduction band minimum of the perovskite.

For measuring charge recombination dynamics, a time-correlated single-photon-counting setup (Edinburgh F900) was applied. Film samples were photoexcited using a 485 nm laser pulsed at frequencies of 2.5 MHz, with a pulse width of 0.7 ns and power of 0.77 mW. The PL light at the wavelength of 770 nm[4] was collected using a high-resolution monochromator.

Theoretical Models and Computational Parameters. First-principles density functional theory calculations were carried out to study the geometry and electronic structure of the perovskite/TiO_2 interface. The static electronic structure and adiabatic molecular dynamics (MD) are performed with the VASP code[61] using a plane wave basis, the PBE density functional,[62,63] and the projector augmented wave (PAW) potentials.[64,65] An energy cutoff of 500 eV and Γ point k-sampling are used. DFT + *U* calculations of Ti 3d electrons are carried out for structural optimization and interfacial dynamics.[66] By applying reliable test of the U value in the range of 3 to 8 eV, we get band gap of 2.9 eV for TiO_2 rutile (110) surface with U = 4.2 eV and J = 0.5 eV, which agrees well with the experimental data (~3.0 eV). It should be noted that the value of U we used is only applicative in our perovskite/TiO_2 system and is not universal for other systems containing Ti atoms.

In line with the experiments, we have placed a perovskite layer on top of rutile TiO_2 (110) surface with stoichiometric composition (Figure 5a). For geometry optimization of bulk TiO_2 and perovskite, a 4 × 4 × 4 Monkhorst−Pack grid was chosen for sampling the Brillouin zone. The calculated lattice constants are a = 6.45 Å and c = 6.495 Å for bulk perovskite $CH_3NH_3PbI_3$; a = 4.66 Å and c = 3.00 Å for bulk rutile-TiO_2. These values are in good agreement with the corresponding experimental ones (a = 6.41 Å and c = 6.415 Å for bulk perovskite; a = 4.59 Å, and c = 2.96 Å for rutile-TiO_2). A (2 × 4) surface slab with 96 atoms in six atomic layers was used to model TiO_2, above which a perovskite sheet containing 84 atoms was included in the calculations. The thickness of the surface vacuum is ~15 Å.

After the static geometry relaxation, we bring the system temperature to 300 K with velocity rescaling. We then carry out MD simulations in the microcanonical ensemble for 1 ps with the MD time-step of 1 fs. The MD trajectory is subsequently used in the NAMD calculations. To determine interfacial electron transfer dynamics, 300 short MD trajectories—each with 100 fs long for electron injection and 150 fs long for charge recombination—are included in the ensemble average; the averaging turns out to be crucial for capturing the stochastic nature of the coupled electron−ion dynamics. For each trajectory, the TDDFT equation is integrated with a time-step of 10^{-3} fs. For the interfacial electron injection dynamics, the initial photoexcited state is chosen from the low-lying empty states with the largest localization on the perovskite layer. On the other hand, for the electron−hole recombination dynamics, the conduction band minimum of TiO_2 is selected as the initial state for the electron while the hole is always sitting in the valence bands of the perovskite.

■ ASSOCIATED CONTENT

Supporting Information

The Supporting Information is available free of charge on the ACS Publications website at DOI: 10.1021/acs.chemmater.5b04019.

XRD spectra for nanocrystalline TiO_2 and compact TiO_2 layer with different V_O densities; SEM image of perovskite nanocrystals; and time-resolved PL measurements of perovskite on different nanocrystalline substrates (PDF)

■ AUTHOR INFORMATION

Corresponding Authors

*E-mail: smeng@iphy.ac.cn. Tel.: + 86-10-82649396.
*E-mail: hguo@iphy.ac.cn.
*E-mail: gang.lu.35@csun.edu.

Author Contributions

¶F.Z. and W.M. contributed equally.

Notes

The authors declare no competing financial interest.

■ ACKNOWLEDGMENTS

We are grateful to Xiao Guo of Institute of Physics, Chinese Academy of Sciences in electrical resistivity measurement. We thank You Li of Peking University for assistance in PL

DOI: 10.1021/acs.chemmater.5b04019
Chem. Mater. 2016, 28, 802−812

measurement. This work was supported by the National Key Basic Research Program of China (Grant Nos. 2012CB921403, 2015CB921001), the National Natural Science Foundation of China (Grant Nos. 11222431, and 11574365), and the Strategic Priority Research Program (B) of the Chinese Academy of Sciences (Grant No. XDB07030100). The work at California State University Northridge was supported by the US National Science Foundation and the Army Research Office.

REFERENCES

(1) Burschka, J.; Pellet, N.; Moon, S.-J.; Humphry-Baker, R.; Gao, P.; Nazeeruddin, M. K.; Gratzel, M. Sequential deposition as a route to high-performance perovskite-sensitized solar cells. *Nature* **2013**, *499*, 316−319.

(2) Kim, H. S.; Lee, C. R.; Im, J. H.; Lee, K. B.; Moehl, T.; Marchioro, A.; Moon, S. J.; Humphry-Baker, R.; Yum, J. H.; Moser, J. E.; Gratzel, M.; Park, N. G. Lead iodide perovskite sensitized all-solid-state submicron thin film mesoscopic solar cell with efficiency exceeding 9%. *Sci. Rep.* **2012**, *2*, 591.

(3) Liu, M.; Johnston, M. B.; Snaith, H. J. Efficient planar heterojunction perovskite solar cells by vapour deposition. *Nature* **2013**, *501*, 395−398.

(4) Stranks, S. D.; Eperon, G. E.; Grancini, G.; Menelaou, C.; Alcocer, M. J. P.; Leijtens, T.; Herz, L. M.; Petrozza, A.; Snaith, H. J. Electron-Hole Diffusion Lengths Exceeding 1 Micrometer in an Organometal Trihalide Perovskite Absorber. *Science* **2013**, *342*, 341−344.

(5) Xing, G.; Mathews, N.; Sun, S.; Lim, S. S.; Lam, Y. M.; Grätzel, M.; Mhaisalkar, S.; Sum, T. C. Long-Range Balanced Electron- and Hole-Transport Lengths in Organic-Inorganic $CH_3NH_3PbI_3$. *Science* **2013**, *342*, 344−347.

(6) Snaith, H. J. Perovskites: The Emergence of a New Era for Low-Cost, High-Efficiency Solar Cells. *J. Phys. Chem. Lett.* **2013**, *4*, 3623−3630.

(7) Hao, F.; Stoumpos, C. C.; Chang, R. P. H.; Kanatzidis, M. G. Anomalous Band Gap Behavior in Mixed Sn and Pb Perovskites Enables Broadening of Absorption Spectrum in Solar Cells. *J. Am. Chem. Soc.* **2014**, *136*, 8094−8099.

(8) Pang, S.; Hu, H.; Zhang, J.; Lv, S.; Yu, Y.; Wei, F.; Qin, T.; Xu, H.; Liu, Z.; Cui, G. $NH_2CH{=}NH_2PbI_3$: An Alternative Organolead Iodide Perovskite Sensitizer for Mesoscopic Solar Cells. *Chem. Mater.* **2014**, *26*, 1485−1491.

(9) Qin, P.; Tanaka, S.; Ito, S.; Tetreault, N.; Manabe, K.; Nishino, H.; Nazeeruddin, M. K.; Gratzel, M. Inorganic hole conductor-based lead halide perovskite solar cells with 12.4% conversion efficiency. *Nat. Commun.* **2014**, *5*, 3834.

(10) Noh, J. H.; Im, S. H.; Heo, J. H.; Mandal, T. N.; Seok, S. I. Chemical Management for Colorful, Efficient, and Stable Inorganic−Organic Hybrid Nanostructured Solar Cells. *Nano Lett.* **2013**, *13*, 1764−1769.

(11) Xiao, M.; Huang, F.; Huang, W.; Dkhissi, Y.; Zhu, Y.; Etheridge, J.; Gray-Weale, A.; Bach, U.; Cheng, Y.-B.; Spiccia, L. A Fast Deposition-Crystallization Procedure for Highly Efficient Lead Iodide Perovskite Thin-Film Solar Cells. *Angew. Chem., Int. Ed.* **2014**, *53*, 9898−9903.

(12) Leyden, M. R.; Ono, L. K.; Raga, S. R.; Kato, Y.; Wang, S.; Qi, Y. High performance perovskite solar cells by hybrid chemical vapor deposition. *J. Mater. Chem. A* **2014**, *2*, 18742−18745.

(13) Nie, W.; Tsai, H.; Asadpour, R.; Blancon, J.-C.; Neukirch, A. J.; Gupta, G.; Crochet, J. J.; Chhowalla, M.; Tretiak, S.; Alam, M. A.; Wang, H.-L.; Mohite, A. D. High-efficiency solution-processed perovskite solar cells with millimeter-scale grains. *Science* **2015**, *347*, 522−525.

(14) Mei, A.; Li, X.; Liu, L.; Ku, Z.; Liu, T.; Rong, Y.; Xu, M.; Hu, M.; Chen, J.; Yang, Y.; Grätzel, M.; Han, H. A hole-conductor−free, fully printable mesoscopic perovskite solar cell with high stability. *Science* **2014**, *345*, 295−298.

(15) O'Mahony, F. T. F.; Lee, Y. H.; Jellett, C.; Dmitrov, S.; Bryant, D. T. J.; Durrant, J. R.; O'Regan, B. C.; Graetzel, M.; Nazeeruddin, M. K.; Haque, S. A. Improved environmental stability of organic lead trihalide perovskite-based photoactive-layers in the presence of mesoporous TiO_2. *J. Mater. Chem. A* **2015**, *3*, 7219−7223.

(16) Jeon, N. J.; Noh, J. H.; Yang, W. S.; Kim, Y. C.; Ryu, S.; Seo, J.; Seok, S. I. Compositional engineering of perovskite materials for high-performance solar cells. *Nature* **2015**, *517*, 476−480.

(17) Zhang, Y.; Liu, M.; Eperon, G. E.; Leijtens, T. C.; McMeekin, D.; Saliba, M.; Zhang, W.; de Bastiani, M.; Petrozza, A.; Herz, L. M.; Johnston, M. B.; Lin, H.; Snaith, H. J. Charge selective contacts, mobile ions and anomalous hysteresis in organic-inorganic perovskite solar cells. *Mater. Horiz.* **2015**, *2*, 315−322.

(18) Kim, H.-S.; Park, N.-G. Parameters Affecting I−V Hysteresis of $CH_3NH_3PbI_3$ Perovskite Solar Cells: Effects of Perovskite Crystal Size and Mesoporous TiO_2 Layer. *J. Phys. Chem. Lett.* **2014**, *5*, 2927−2934.

(19) Chen, H.-W.; Sakai, N.; Ikegami, M.; Miyasaka, T. Emergence of Hysteresis and Transient Ferroelectric Response in Organo-Lead Halide Perovskite Solar Cells. *J. Phys. Chem. Lett.* **2015**, *6*, 164−169.

(20) Kutes, Y.; Ye, L.; Zhou, Y.; Pang, S.; Huey, B. D.; Padture, N. P. Direct Observation of Ferroelectric Domains in Solution-Processed $CH_3NH_3PbI_3$ Perovskite Thin Films. *J. Phys. Chem. Lett.* **2014**, *5*, 3335−3339.

(21) Frost, J. M.; Butler, K. T.; Brivio, F.; Hendon, C. H.; van Schilfgaarde, M.; Walsh, A. Atomistic Origins of High-Performance in Hybrid Halide Perovskite Solar Cells. *Nano Lett.* **2014**, *14*, 2584−2590.

(22) Beilsten-Edmands, J.; Eperon, G. E.; Johnson, R. D.; Snaith, H. J.; Radaelli, P. G. Non-ferroelectric nature of the conductance hysteresis in $CH_3NH_3PbI_3$ perovskite-based photovoltaic devices. *Appl. Phys. Lett.* **2015**, *106*, 173502.

(23) Eames, C.; Frost, J. M.; Barnes, P. R.; O'Regan, B. C.; Walsh, A.; Islam, M. S. Ionic transport in hybrid lead iodide perovskite solar cells. *Nat. Commun.* **2015**, *6*, 7497.

(24) Eperon, G. E.; Paterno, G. M.; Sutton, R. J.; Zampetti, A.; Haghighirad, A. A.; Cacialli, F.; Snaith, H. J. Inorganic caesium lead iodide perovskite solar cells. *J. Mater. Chem. A* **2015**, *3*, 19688−19695.

(25) Tress, W.; Marinova, N.; Moehl, T.; Zakeeruddin, S. M.; Nazeeruddin, M. K.; Gratzel, M. Understanding the rate-dependent J-V hysteresis, slow time component, and aging in $CH_3NH_3PbI_3$ perovskite solar cells: the role of a compensated electric field. *Energy Environ. Sci.* **2015**, *8*, 995−1004.

(26) Shao, Y.; Xiao, Z.; Bi, C.; Yuan, Y.; Huang, J. Origin and elimination of photocurrent hysteresis by fullerene passivation in $CH_3NH_3PbI_3$ planar heterojunction solar cells. *Nat. Commun.* **2014**, *5*, 5784.

(27) Xiao, Z.; Bi, C.; Shao, Y.; Dong, Q.; Wang, Q.; Yuan, Y.; Wang, C.; Gao, Y.; Huang, J. Efficient, High Yield Perovskite Photovoltaic Devices Grown by Interdiffusion of Solution-Processed Precursor Stacking Layers. *Energy Environ. Sci.* **2014**, *7*, 2619−2623.

(28) Xu, J.; Buin, A.; Ip, A. H.; Li, W.; Voznyy, O.; Comin, R.; Yuan, M.; Jeon, S.; Ning, Z.; McDowell, J. J.; Kanjanaboos, P.; Sun, J.-P.; Lan, X.; Quan, L. N.; Kim, D. H.; Hill, I. G.; Maksymovych, P.; Sargent, E. H. Perovskite-fullerene hybrid materials suppress hysteresis in planar diodes. *Nat. Commun.* **2015**, *6*, 7081.

(29) Zhao, Y.; Liang, C.; Zhang, H.; Li, D.; Tian, D.; Li, G.; Jing, X.; Zhang, W.; Xiao, W.; Liu, Q.; Zhang, F.; He, Z. Anomalously large interface charge in polarity-switchable photovoltaic devices: an indication of mobile ions in organic-inorganic halide perovskites. *Energy Environ. Sci.* **2015**, *8*, 1256−1260.

(30) Xiao, Z.; Yuan, Y.; Shao, Y.; Wang, Q.; Dong, Q.; Bi, C.; Sharma, P.; Gruverman, A.; Huang, J. Giant switchable photovoltaic effect in organometal trihalide perovskite devices. *Nat. Mater.* **2015**, *14*, 193−198.

(31) van Reenen, S.; Kemerink, M.; Snaith, H. J. Modeling Anomalous Hysteresis in Perovskite Solar Cells. *J. Phys. Chem. Lett.* **2015**, *6*, 3808−3814.

(32) Nagaoka, H.; Ma, F.; deQuilettes, D. W.; Vorpahl, S. M.; Glaz, M. S.; Colbert, A. E.; Ziffer, M. E.; Ginger, D. S. Zr Incorporation into

DOI: 10.1021/acs.chemmater.5b04019
Chem. Mater. 2016, 28, 802−812

TiO_2 Electrodes Reduces Hysteresis and Improves Performance in Hybrid Perovskite Solar Cells while Increasing Carrier Lifetimes. *J. Phys. Chem. Lett.* **2015**, *6*, 669−675.
(33) Heo, J. H.; You, M. S.; Chang, M. H.; Yin, W.; Ahn, T. K.; Lee, S.-J.; Sung, S.-J.; Kim, D. H.; Im, S. H. Hysteresis-less mesoscopic $CH_3NH_3PbI_3$ perovskite hybrid solar cells by introduction of Li-treated TiO_2 electrode. *Nano Energy* **2015**, *15*, 530−539.
(34) Li, Z.; Zhang, X.; Lu, G. Dipole-Assisted Charge Separation in Organic−Inorganic Hybrid Photovoltaic Heterojunctions: Insight from First-Principles Simulations. *J. Phys. Chem. C* **2012**, *116*, 9845−9851.
(35) Li, Z.; Zhang, X.; Lu, G. Electron Dynamics in Dye-Sensitized Solar Cells: Effects of Surface Terminations and Defects. *J. Phys. Chem. B* **2010**, *114*, 17077−17083.
(36) Guo, H. Z.; Chen, Z. H.; Cheng, B. L.; Lu, H. B.; Liu, L. F.; Zhou, Y. L. Structure dynamics of strongly reduced epitaxial $BaTiO_{3-x}$ studied by Raman scattering. *J. Eur. Ceram. Soc.* **2005**, *25*, 2347−2352.
(37) Guo, H. Z.; Burgess, J.; Ada, E.; Street, S.; Gupta, A.; Iliev, M. N.; Kellock, A. J.; Magen, C.; Varela, M.; Pennycook, S. J. Influence of defects on structural and magnetic properties of multifunctional La_2NiMnO_6 thin films. *Phys. Rev. B: Condens. Matter Mater. Phys.* **2008**, *77*, 174423.
(38) Nowotny, M. K.; Bak, T.; Nowotny, J. Electrical Properties and Defect Chemistry of TiO_2 Single Crystal. I. Electrical Conductivity. *J. Phys. Chem. B* **2006**, *110*, 16270−16282.
(39) Kim, Y.; Yoo, B. J.; Vittal, R.; Lee, Y.; Park, N.-G.; Kim, K.-J. Low-temperature oxygen plasma treatment of TiO_2 film for enhanced performance of dye-sensitized solar cells. *J. Power Sources* **2008**, *175*, 914−919.
(40) Ishida, N.; Fujita, D. Superhydrophilic TiO_2 surfaces generated by reactive oxygen treatment. *J. Vac. Sci. Technol., A* **2012**, *30*, 051402.
(41) Zhang, Y.; Ma, X.; Chen, P.; Li, D.; Pi, X.; Yang, D.; Coleman, P. G. Enhancement of electroluminescence from TiO2/p+-Si heterostructure-based devices through engineering of oxygen vacancies in TiO_2. *Appl. Phys. Lett.* **2009**, *95*, 252102.
(42) Luo, Z.; Jiang, H.; Li, D.; Hu, L.; Geng, W.; Wei, P.; Ouyang, P. Improved photocatalytic activity and mechanism of Cu_2O/N-TiO_2 prepared by a two-step method. *RSC Adv.* **2014**, *4*, 17797−17804.
(43) Sheehan, S.; Ravindranathan Thampi, K.; Dowling, D. P. Influence of microwave plasma pre-treatments of TiO_2 electrodes on dye-sensitised solar cell efficiencies. *J. Electroanal. Chem.* **2014**, *725*, 12−18.
(44) Snaith, H. J.; Abate, A.; Ball, J. M.; Eperon, G. E.; Leijtens, T.; Noel, N. K.; Stranks, S. D.; Wang, J. T.-W.; Wojciechowski, K.; Zhang, W. Anomalous Hysteresis in Perovskite Solar Cells. *J. Phys. Chem. Lett.* **2014**, *5*, 1511−1515.
(45) Piatkowski, P.; Cohen, B.; Javier Ramos, F.; Di Nunzio, M.; Nazeeruddin, M. K.; Gratzel, M.; Ahmad, S.; Douhal, A. Direct monitoring of ultrafast electron and hole dynamics in perovskite solar cells. *Phys. Chem. Chem. Phys.* **2015**, *17*, 14674−14684.
(46) Lee, M. M.; Teuscher, J.; Miyasaka, T.; Murakami, T. N.; Snaith, H. J. Efficient Hybrid Solar Cells Based on Meso-Superstructured Organometal Halide Perovskites. *Science* **2012**, *338*, 643−647.
(47) Wang, L.; McCleese, C.; Kovalsky, A.; Zhao, Y.; Burda, C. Femtosecond Time-Resolved Transient Absorption Spectroscopy of $CH_3NH_3PbI_3$ Perovskite Films: Evidence for Passivation Effect of PbI_2. *J. Am. Chem. Soc.* **2014**, *136*, 12205−12208.
(48) deQuilettes, D. W.; Vorpahl, S. M.; Stranks, S. D.; Nagaoka, H.; Eperon, G. E.; Ziffer, M. E.; Snaith, H. J.; Ginger, D. S. Impact of microstructure on local carrier lifetime in perovskite solar cells. *Science* **2015**, *348*, 683−686.
(49) Dong, Q.; Fang, Y.; Shao, Y.; Mulligan, P.; Qiu, J.; Cao, L.; Huang, J. Electron-hole diffusion lengths > 175 μm in solution grown $CH_3NH_3PbI_3$ single crystals. *Science* **2015**, *347*, 967−970.
(50) Xing, G.; Wu, B.; Chen, S.; Chua, J.; Yantara, N.; Mhaisalkar, S.; Mathews, N.; Sum, T. C. Interfacial Electron Transfer Barrier at Compact TiO_2/$CH_3NH_3PbI_3$ Heterojunction. *Small* **2015**, *11*, 3606−3613.
(51) Cheng, H.; Selloni, A. Surface and subsurface oxygen vacancies in anatase TiO_2 and differences with rutile. *Phys. Rev. B: Condens. Matter Mater. Phys.* **2009**, *79*, 092101.
(52) Cho, E.; Han, S.; Ahn, H.-S.; Lee, K.-R.; Kim, S. K.; Hwang, C. S. First-principles study of point defects in rutile TiO_2. *Phys. Rev. B: Condens. Matter Mater. Phys.* **2006**, *73*, 193202.
(53) Janotti, A.; Varley, J. B.; Rinke, P.; Umezawa, N.; Kresse, G.; Van de Walle, C. G. Hybrid functional studies of the oxygen vacancy in TiO_2. *Phys. Rev. B: Condens. Matter Mater. Phys.* **2010**, *81*, 085212.
(54) Krüger, P.; Bourgeois, S.; Domenichini, B.; Magnan, H.; Chandesris, D.; Le Fèvre, P.; Flank, A. M.; Jupille, J.; Floreano, L.; Cossaro, A.; Verdini, A.; Morgante, A. Defect States at the TiO_2(110) Surface Probed by Resonant Photoelectron Diffraction. *Phys. Rev. Lett.* **2008**, *100*, 055501.
(55) Kwon, J.; Sharma, A. A.; Bain, J. A.; Picard, Y. N.; Skowronski, M. Oxygen Vacancy Creation, Drift, and Aggregation in TiO_2-Based Resistive Switches at Low Temperature and Voltage. *Adv. Funct. Mater.* **2015**, *25*, 2876−2883.
(56) Miyaoka, H.; Mizutani, G.; Sano, H.; Omote, M.; Nakatsuji, K.; Komori, F. Anomalous electro-migration of oxygen vacancies in reduced TiO_2. *Solid State Commun.* **2002**, *123*, 399−404.
(57) Li, D.; Li, M.; Zahid, F.; Wang, J.; Guo, H. Oxygen vacancy filament formation in TiO_2: A kinetic Monte Carlo study. *J. Appl. Phys.* **2012**, *112*, 073512.
(58) Yang, Y.; Yang, M.; Li, Z.; Crisp, R.; Zhu, K.; Beard, M. C. Comparison of Recombination Dynamics in $CH_3NH_3PbBr_3$ and $CH_3NH_3PbI_3$ Perovskite Films: Influence of Exciton Binding Energy. *J. Phys. Chem. Lett.* **2015**, *6*, 4688−4692.
(59) Wen, X.; Sheng, R.; Ho-Baillie, A. W. Y.; Benda, A.; Woo, S.; Ma, Q.; Huang, S.; Green, M. A. Morphology and Carrier Extraction Study of Organic−Inorganic Metal Halide Perovskite by One and Two-Photon Fluorescence Microscopy. *J. Phys. Chem. Lett.* **2014**, *5*, 3849−3853.
(60) Yamada, Y.; Yamada, T.; Phuong, L. Q.; Maruyama, N.; Nishimura, H.; Wakamiya, A.; Murata, Y.; Kanemitsu, Y. Dynamic Optical Properties of $CH_3NH_3PbI_3$ Single Crystals As Revealed by One- and Two-Photon Excited Photoluminescence Measurements. *J. Am. Chem. Soc.* **2015**, *137*, 10456−10459.
(61) Kresse, G.; Furthmüller, J. Efficient iterative schemes for ab-initio total-energy calculations using a plane-wave basis set. *Phys. Rev. B: Condens. Matter Mater. Phys.* **1996**, *54*, 11169−11186.
(62) Perdew, J. P.; Burke, K.; Ernzerhof, M. Generalized Gradient Approximation Made Simple. *Phys. Rev. Lett.* **1996**, *77*, 3865−3868.
(63) Perdew, J. P.; Burke, K.; Ernzerhof, M. Generalized Gradient Approximation Made Simple [Phys. Rev. Lett. 77, 3865 (1996)]. *Phys. Rev. Lett.* **1997**, *78*, 1396−1396.
(64) Blöchl, P. E. Projector augmented-wave method. *Phys. Rev. B: Condens. Matter Mater. Phys.* **1994**, *50*, 17953−17979.
(65) Kresse, G.; Joubert, D. From ultrasoft pseudopotentials to the projector augmented-wave method. *Phys. Rev. B: Condens. Matter Mater. Phys.* **1999**, *59*, 1758−1775.
(66) Umari, P.; Mosconi, E.; De Angelis, F. Relativistic GW calculations on $CH_3NH_3PbI_3$ and $CH_3NH_3SnI_3$ perovskites for solar cell applications. *Sci. Rep.* **2014**, *4*, 4467.

DOI: 10.1021/acs.chemmater.5b04019
Chem. Mater. 2016, 28, 802−812